



Preparation of carbon-coated MnCO₃@MnO₂ hierarchical hollow nanostructure and their application in supercapacitors

Meijiao Sun¹, Zhenkun Zhang¹, Xiaoqiang Wang¹, Yifan Tan¹, Shuixin Xia¹, Yuhua Xue¹, and Guangzhi Yang^{1,*}

¹ School of Materials Science and Engineering, University of Shanghai for Science and Technology, Shanghai 200093, China

Received: 23 June 2021

Accepted: 26 October 2021

Published online:

1 November 2021

© The Author(s), under exclusive licence to Springer Science+Business Media, LLC, part of Springer Nature 2021

ABSTRACT

The rational structure design of the electrode materials is critical to achieve high-performance supercapacitors. In this contribution, a structure of carbon-coated MnCO₃@MnO₂ (MnCO₃@MnO₂@C) hierarchical hollow nanostructures is obtained through redox reaction on the basis of Kirkendall effect. The hollow structure and the coating of carbon layer provides a space and utilization rate of materials for charge storage in electrochemical energy storage. The electrode demonstrates an electrochemical performance with a specific capacitance of 267 F g⁻¹ and a retention rate of 83.6% after 8000 cycles at 1A g⁻¹. When the MnCO₃@MnO₂@C is used as positive electrode combined with hollow carbon sphere as the negative electrode, the assembled asymmetric supercapacitor displays a power density of 3840 Wkg⁻¹ and energy density of 21.3 Wh kg⁻¹, 78.2% of capacitance retention after 5000 cycles at 2 A g⁻¹.

1 Introduction

Supercapacitors (SC), also known as electrochemical supercapacitors, have a variety of priorities when used for energy storage device, such as high power density, high safety, long cycle life, low cost, and good performance stability and so on [1]. Its high specific capacity and energy density are due to the large electrolyte–electrode contact area, short electrolyte ion transport distance and rapid redox reaction [2]. Generally speaking, supercapacitors are divided into electric double-layer capacitors and pseudo-capacitors according to their energy storage

mechanism [3, 4]. Compared with electric double-layer capacitors, pseudo-capacitors have reversible electron transfer capabilities between the oxidized state and the reduced state. The energy storage mechanism relies on not only the electric double layer capacitance of the electrode material, but also the rapid redox reaction between the electrode material itself and the electrolyte ions to achieve energy storage [5].

The electrochemical performance of pseudo-capacitors depends on the active electrode materials used, including metal oxides (Co₃O₄, SnO₂, MnO₂, Fe₂O₃) [4, 6] and conductive polymers (polypyrrole

Address correspondence to E-mail: yanggzhi@usst.edu.cn

and polyaniline) [7–10]. These materials have mesoporous structures of high-specific surface area and uniform pore size distribution, which makes them promising when used for capacitors [11]. MnO_2 has become one of the most attractive positive electrode candidates due to its rich content, low cost, and high theoretical-specific capacitance [12, 13]. However, like other metal oxides, MnO_2 has inherent shortcomings such as small ion diffusion constant, poor conductivity, and easy expansion and pulverization during the cycle, making its energy storage effect difficult to obtain the ideal specific capacity [14]. The most common way to solve these problems is to composite MnO_2 with other materials to combine the advantages of each constitutes to achieve highly effective energy storage. In addition, conductive polymer, due to high theoretical-specific capacity, excellent electrochemical activity and other characteristics, is a relatively widely used active electrode material for constructing supercapacitors [15]. Polypyrrole (PPY), as one of the conducting polymers, has emerged as a promising active material for high-performance supercapacitors owing to its high electrical conductivity and interesting redox properties [16].

Carbon materials have many prior characteristics when applied in electrochemical energy storage, including large-specific surface area, high conductivity and chemical stability. However, structural optimization will greatly improve the utilizing effects of carbon materials as electrode materials [3, 17]. Hollow structure has the advantages of low density, large surface area, and short charge transfer distance. The local cavity inside the structure can accommodate the large volume changes and delay capacity decay. The large contact area of the electrolysis electrode provides a reasonable idea for the structure design of the electrode materials [6]. Hollow carbon spheres (HCS), due to their various possibilities to be adjusted and controlled in size, pores and specific surface area, can provide abundant space for energy storage, and have attracted many focuses on supercapacitor electrode applications [18, 19].

In this study, carbon-coated $\text{MnCO}_3@ \text{MnO}_2$ ($\text{MnCO}_3@ \text{MnO}_2@ \text{C}$) hierarchical hollow nanostructures were successfully designed and fabricated via a continuous redox reaction of potassium permanganate (KMnO_4) and manganese carbonate (MnCO_3) on the basis of Kirkendall effect. The hierarchical hollow structure composites provide a wealth of

electrochemical active sites and relatively high levels for rapid diffusion and reaction. Moreover, the coating of the outer carbon layer facilitate the effective contact between the electrode material and the electrolyte, which will greatly improve the electrochemical performance of the electrode material. When the $\text{MnCO}_3@ \text{MnO}_2@ \text{C}$ (as the positive electrode) and HCS (as the negative electrode) were used to assemble an asymmetric supercapacitors device, the capacitors remained 78.2% of the capacitance retention after 5000 cycles, and the coulombic efficiency is close to 100%.

2 Experimental

2.1 Preparation of $\text{MnCO}_3@ \text{MnO}_2@ \text{C}$

2.1.1 Preparation of $\text{MnCO}_3@ \text{MnO}_2$

First, 7 ml of ethanol and manganese sulfate (MnSO_4) aqueous solution (1.0 g of MnSO_4 dissolved in 70 ml of deionized water) were mixed thoroughly via stirring. Then sodium bicarbonate (NaHCO_3) aqueous solution (2.5 g of NaHCO_3 dissolve in 70 ml of deionized water) and 25 μl of ammonia solution were added and stirred continuously for 2 h. Finally, MnCO_3 microspheres were obtained after washed and dried.

$\text{MnCO}_3@ \text{MnO}_2$ hierarchical hollow spheres were prepared by controlled reaction of KMnO_4 and MnCO_3 on the basis of Kirkendall effect, which is based on the atomic interface diffusion motion at the boundary due to the different diffusion rates of metal atoms [20–22]. First, 0.5 g of MnCO_3 microspheres were added into 70 ml of deionized water and ultrasonically dispersed by cell crusher. Then, the potassium permanganate (KMnO_4) solution (0.86 g of KMnO_4 dissolved in 100 ml of deionized water) were added and stirred for 2 h. The obtained precipitate was washed to neutrality by centrifugation and then dried to obtain hierarchical $\text{MnCO}_3@ \text{MnO}_2$. The samples were then dispersed into 150 ml of 0.1 M hydrochloric acid and stirred to remove MnCO_3 . Finally, the samples were washed to neutrality to obtain hierarchical hollow nanostructure $\text{MnCO}_3@ \text{MnO}_2$.

2.1.2 Preparation of hierarchical hollow nanostructure $\text{MnCO}_3@\text{MnO}_2@\text{C}$

100 mg of $\text{MnCO}_3@\text{MnO}_2$ samples were dispersed in 40 ml of deionized water via ultrasonic agitation. Then, 10 mg of ammonium persulfate was dissolved in 20 ml of 5 vol% pyrrole (PPY) solution, the mixed solutions were dropwise added into the above-mentioned $\text{MnCO}_3@\text{MnO}_2$ solutions, and stirred continuously for 4 h under ice bath conditions. After being washed under centrifugation and then dried, the obtained samples of $\text{MnCO}_3@\text{MnO}_2@\text{PPY}$ were carbonized to obtain hierarchical hollow nanostructure $\text{MnCO}_3@\text{MnO}_2@\text{C}$.

2.2 Preparation of HCS

3.46 ml of tetrapropyl orthosilicate (TPOS) was added and stirred to the mixture of ethanol (70 ml), deionized water (10 ml), and ammonia (3 ml). After 15 min, 0.4 g of resorcinol and 0.56 ml of formaldehyde were added. After being stirred for 24 h, the as-prepared sample was washed under centrifugation, dried, carbonized, and etched with sodium hydroxide to obtain HCS.

2.3 Materials characterization

The structure and morphology of the sample were analyzed by Fourier transform infrared (FTIR, Spectrum100: Perkin Elmer), X-ray diffraction (XRD, D8 Advance: Bruker), field emission scanning electron microscope (FE-SEM, QUANTA FEG 450: FEI), transmission electron microscope (TEM, TECNAI F30: FEI), and Energy spectrometer (EDS, APOLLO X: AMETEK Group) to analyze the element content of the sample.

2.4 Electrochemical performance analysis

The working electrode was fabricated by painting the slurry onto nickel foam of 1.0 cm^2 with isopropanol as dispersion solvent, which consists of 80 wt% active material, 10 wt% carbon black and 10 wt% polyvinylidene fluoride (PVDF) as binder. Subsequently, the prepared electrodes were heated in a vacuum oven at $90 \text{ }^\circ\text{C}$ for 12 h and then pressed for 120 s under a pressure of 6 MPa. The electrochemical performance of the electrodes is tested by electrochemical workstation (CHI760D, Shanghai Chenhua

Co. Ltd. China) with a three-electrode cell in a 2 M KOH aqueous solution. The sample serves as the working electrodes, Platinum electrode as the counter electrode, and the Hg/HgO electrodes as the reference electrode, respectively. Cyclic voltammetry (CV), galvanostatic charge and discharge (GCD), and electrochemical impedance spectroscopy (EIS) methods were carried out to characterize the electrochemical performance of as-prepared samples, including specific capacitance, redox reactions, reversibility and cycling stability. The specific capacitance ($C, \text{F g}^{-1}$) can be calculated from the CV curves according to the following equation [23]:

$$C = \frac{A}{2sm\Delta V} \quad (1)$$

where, A is the integral areas of the CV curve, m (g) is the average mass of electrode material, ΔV (V) is the potential window, s ($\text{mV}\cdot\text{s}^{-1}$) is the potential scan rate.

The specific capacitance ($C, \text{F g}^{-1}$), power density ($P, \text{Wh kg}^{-1}$) and energy density ($E, \text{W kg}^{-1}$) can be calculated from the GCD curves according to the following equation [24, 25]:

$$C = \frac{I\Delta t}{m\Delta V} \quad (2)$$

$$E = \frac{CV^2}{2 \times 3.6} \quad (3)$$

$$P = \frac{E}{\Delta t} \times 3600 \quad (4)$$

where, I (A) and Δt (s) is the current loaded and the discharge time during GCD process, m (g) and ΔV (V) is the mass of the electrode material and the potential window, respectively.

3 Results and discussion

3.1 Structure and morphology analysis

Figure 1 is the synthesis schematic diagram of the hierarchical hollow nanostructure $\text{MnCO}_3@\text{MnO}_2@\text{C}$ composite. Firstly, using monodisperse MnCO_3 microspheres as a template, KMnO_4 is involved in the reaction to form $\text{MnCO}_3@\text{MnO}_2$, and then the remaining MnCO_3 is reacted with hydrochloric acid to form $\text{MnCO}_3@\text{MnO}_2$ with a hierarchical hollow structure. The reaction principle of the Kirkendall effect, it involves in this step, the motion formation of

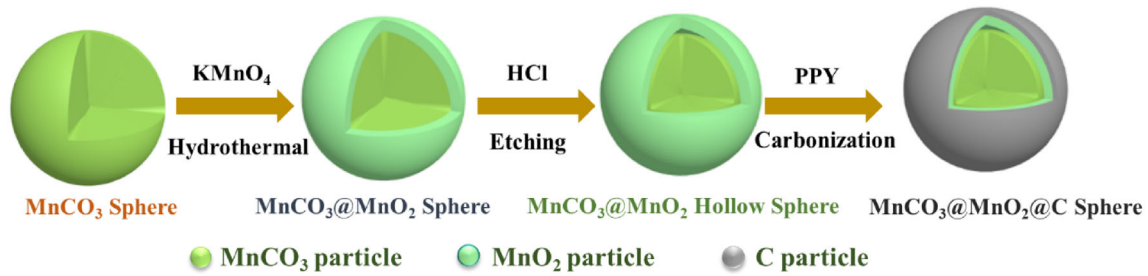


Fig. 1 Schematic diagram of the hierarchical hollow nanostructure $\text{MnCO}_3@\text{MnO}_2@\text{C}$ composite

diffusion pairs at the interface between KMnO_4 and MnCO_3 might lead to the rapid formation of MnO_2 shells on the outer surface of MnCO_3 crystals. The $\text{MnCO}_3@\text{MnO}_2$ hierarchical hollow nanostructure will be formed after the removal of the MnCO_3 crystal cores by HCl [20, 22]. Finally, PPY is used as a carbon precursor to coat the $\text{MnCO}_3@\text{MnO}_2$ microspheres to form $\text{MnCO}_3@\text{MnO}_2@\text{PPY}$. It is transformed into $\text{MnCO}_3@\text{MnO}_2@\text{C}$ composites by carbonization.

Figure 2a is the FTIR spectrum of $\text{MnCO}_3@\text{MnO}_2$, PPY, $\text{MnCO}_3@\text{MnO}_2@\text{PPY}$ and $\text{MnCO}_3@\text{MnO}_2@\text{C}$ composites in the range of $450\text{--}4000\text{ cm}^{-1}$. The gray curve and black curve correspond to the infrared spectra of pure PPY and $\text{MnCO}_3@\text{MnO}_2@\text{PPY}$ respectively, where the absorption peaks at $1549, 1458, 1312, 1176$ and 680 cm^{-1} belong to the basic vibration of PPY, the stretching vibration of the C–N bond and the deformation vibration of = C–H. These

are consistent with reports on PPY in the literature [26], indicating that PPY was successfully coated on the surface of $\text{MnCO}_3@\text{MnO}_2$ microspheres. In addition, a characteristic absorption peak at 528 cm^{-1} in manganese dioxide is the Mn–O stretching vibration absorption peak, indicating that manganese dioxide is present in the prepared composite material [27]. In the material of $\text{MnCO}_3@\text{MnO}_2@\text{C}$, the characteristic peak of PPY disappears and a weak peak at 1327 cm^{-1} of bending vibration of C = N appears, indicating that PPY was transformed into amorphous carbon.

To determine the composition of the prepared samples, XRD analysis was further performed. Figure 2b shows the powder X-ray diffraction patterns of the prepared MnCO_3 , $\text{MnCO}_3@\text{MnO}_2$, $\text{MnCO}_3@\text{MnO}_2@\text{PPY}$, $\text{MnCO}_3@\text{MnO}_2@\text{C}$ samples. The diffraction peaks of MnCO_3 at 2θ of $24^\circ, 31^\circ, 37.5^\circ, 41.4^\circ$, and 51.6° correspond to the five lattice planes of

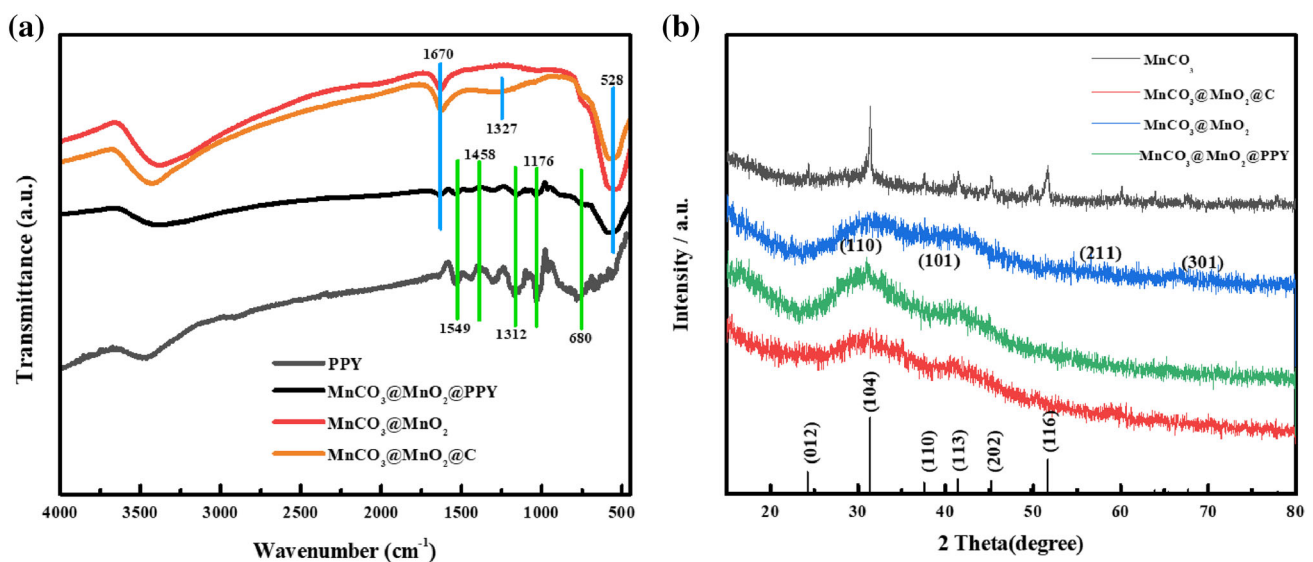


Fig. 2 FT-IR and XRD spectra of the prepared materials: **a** FT-IR, **b** XRD

(012), (104), (110), (113) and (116), respectively, which is consistent with the standard PDF card of MnCO_3 (PDF#44-1472). The broad diffraction peaks of 29.6° , 38.3° , 56.6° , and 72.2° , corresponding to (110), (101), (211), (301) crystal plane, respectively. However, the broad peak shapes are related to a poorly crystallinity, indicating that all composites are amorphous structure [28]. After coating with PPY, it can be seen that the previous characteristic peaks all changed significantly, indicating that the coating is successful. For the carbonized sample $\text{MnCO}_3@ \text{MnO}_2@ \text{C}$, there is an obvious broad diffraction peak at 43° which can be attributed to the reflection of the disordered carbon layer (100) [29].

SEM image in Fig. 3a shows that the prepared MnCO_3 microspheres have homogeneous morphology and good dispersion. In the large magnification of Fig. 3d, it can be seen that the size of the prepared MnCO_3 microspheres is between 700 and 900 nm. Meanwhile, some disordered nanoparticles were found uniformly deposited on the surface of the microspheres. The spectrum in Fig. 2b,e shows that their surface morphology is almost the same as that of MnCO_3 together with good dispersity. However, the diameter of the spheres is about $1 \mu\text{m}$, which increases obviously, indicating that a certain part of MnCO_3 is converted into MnO_2 as a result of reacting with KMnO_4 . SEM image in Fig. 3c and f shows the surface of the $\text{MnCO}_3@ \text{MnO}_2$ spheres is composed of a large number of nanoparticles. Meanwhile, in the low-magnification SEM image, it can be seen that the hierarchical hollow nanostructure of $\text{MnCO}_3@ \text{MnO}_2$ has a uniform morphology and good dispersion. The particle size of the microspheres is between 900 and 1000 nm, which demonstrate that the etching of hydrochloric acid removes some MnCO_3 on the surface and form the hierarchical hollow nanostructures of $\text{MnCO}_3@ \text{MnO}_2$. SEM image in Fig. 3g–h shows that the coated $\text{MnCO}_3@ \text{MnO}_2$ microspheres have uniform morphology and good dispersion. There are microspheres be found inside the broken shell, indicating that it has a core–shell structure. After carbonization treatment, the $\text{MnCO}_3@ \text{MnO}_2@ \text{C}$ composite material is obtained. The size of the microspheres after carbonization decreases, indicating a shrink of volume is caused. While the sphere structure remains intact whose shape is uniform and well dispersed. The element existence of carbon, manganese and oxygen are found by EDS analysis (Fig. 3i), indicating the components of atoms are

consistent with that of $\text{MnCO}_3@ \text{MnO}_2@ \text{C}$. The detailed structural information of the $\text{MnCO}_3@ \text{MnO}_2@ \text{C}$ composites was further investigated by TEM. As shown in Fig. 3j and k, an obvious hollow core–shell structure is observed. It is found that MnCO_3 with dark image and MnO_2 with a little dark image as the main core and shell, respectively. And another relatively thin shell of carbon with grey image could be found surrounding the MnO_2 shell. As indicated in the Fig. 3l, an interlayer spacing of 0.25 nm is found which is marked by the orange line, corresponding to the (101) crystal plane of MnO_2 .

3.2 Electrochemical performance of electrode materials

The electrochemical properties of $\text{MnCO}_3@ \text{MnO}_2$ hollow sphere and $\text{MnCO}_3@ \text{MnO}_2@ \text{C}$ were evaluated in Fig. 4. As presented in Fig. 4 a,d, the relatively regular quasi-rectangular CV curve of $\text{MnCO}_3@ \text{MnO}_2$ and $\text{MnCO}_3@ \text{MnO}_2@ \text{C}$ nanospheres at different scan rates, indicating the as-prepared materials possess an excellent capacitive behavior and reversibility[30]. As the scanning rate increases, the contact time between electrolyte ions and the electrode surface is shortened, and it is difficult for electrolyte ions to enter the interior of the two composite electrode materials, resulting in the deviation of the CV curve and the increase of polarization current which affects its rate capability. At high scanning rate, the contact time between electrolyte ions and the electrode becomes shorter, and the degree of oxidation and reduction will also decrease, which affects the specific capacity. However, compared with $\text{MnCO}_3@ \text{MnO}_2$, the integrated area of $\text{MnCO}_3@ \text{MnO}_2@ \text{C}$ is larger at the same sweep speed, indicating that the current response density is greater. It can be inferred that the composite electrode material coated with carbon has a larger specific capacity. GCD tests of $\text{MnCO}_3@ \text{MnO}_2$ and $\text{MnCO}_3@ \text{MnO}_2@ \text{C}$ at different constant current densities are shown in Fig. 4b, e. The curves of electrode materials are relatively symmetrical triangles, indicating that the composite electrode material has good capacitance characteristics and ideal coulomb efficiency. The $\text{MnCO}_3@ \text{MnO}_2@ \text{C}$ composite electrode material has the longest discharge time, indicating that it has a large specific capacity, which is consistent with the CV curve. With the increase of current density, the discharge time decreases and the voltage

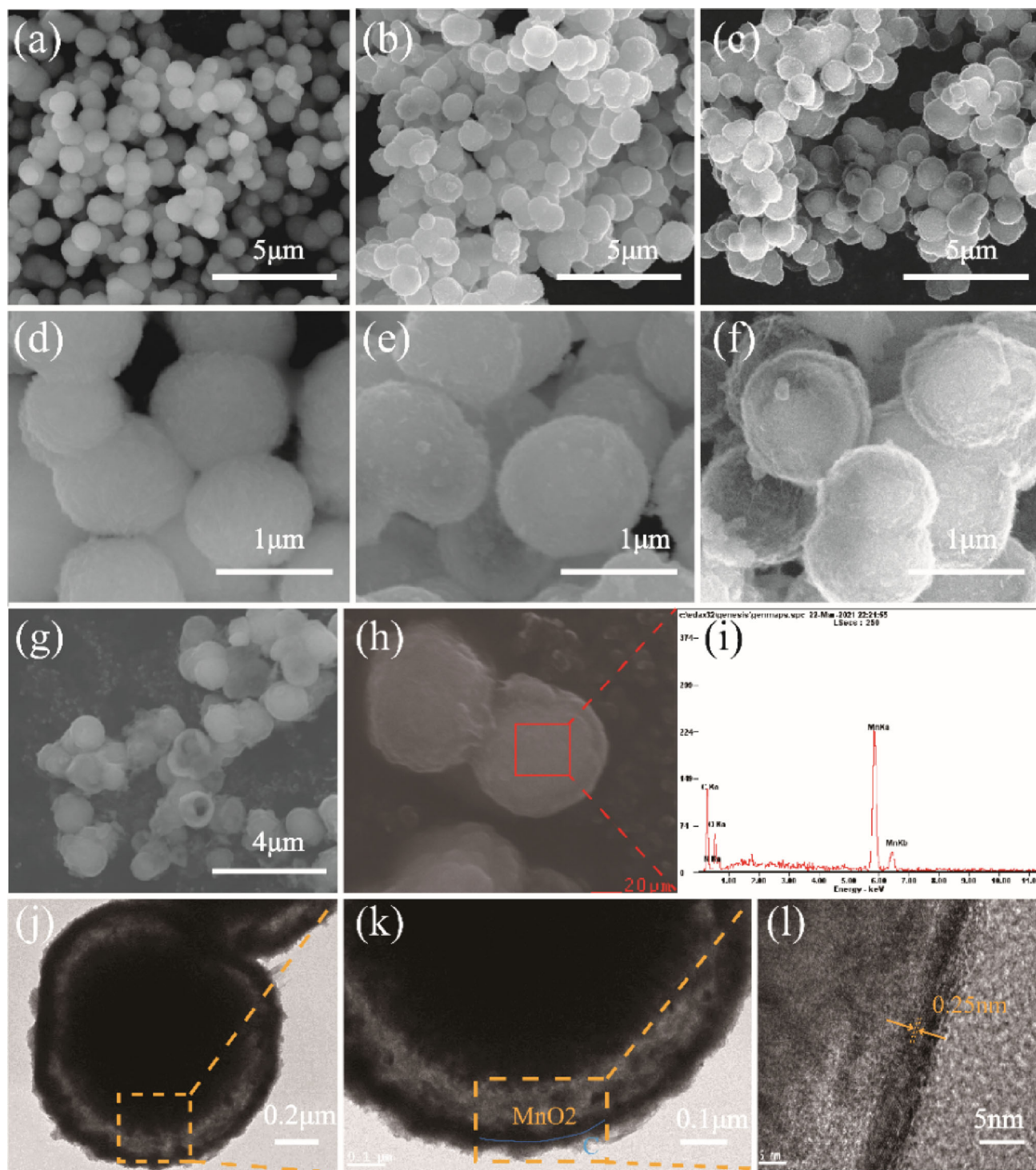


Fig. 3 SEM images of prepared materials **a, d** MnCO_3 , **b, e** $\text{MnCO}_3@MnO_2$, **c, f** Hierarchical hollow $\text{MnCO}_3@MnO_2$, **g** $\text{MnCO}_3@MnO_2@PPY$, **h, i** SEM images and EDS analysis of $\text{MnCO}_3@MnO_2@C$, **j, k, l** TEM images of $\text{MnCO}_3@MnO_2@C$

dropping increases, as a result of interface resistance increase. The spectrum indicates that an irreversible redox reaction between electrolyte and electrode occurs with an ideal capacitance behavior and high

coulomb efficiency. The relationship curve of specific capacitances calculated from Fig. 4b, e and current density is plotted in Fig. 4c, f. For $\text{MnCO}_3@MnO_2$, the specific capacitances is $246 \text{ F} \cdot \text{g}^{-1}$ at current density of

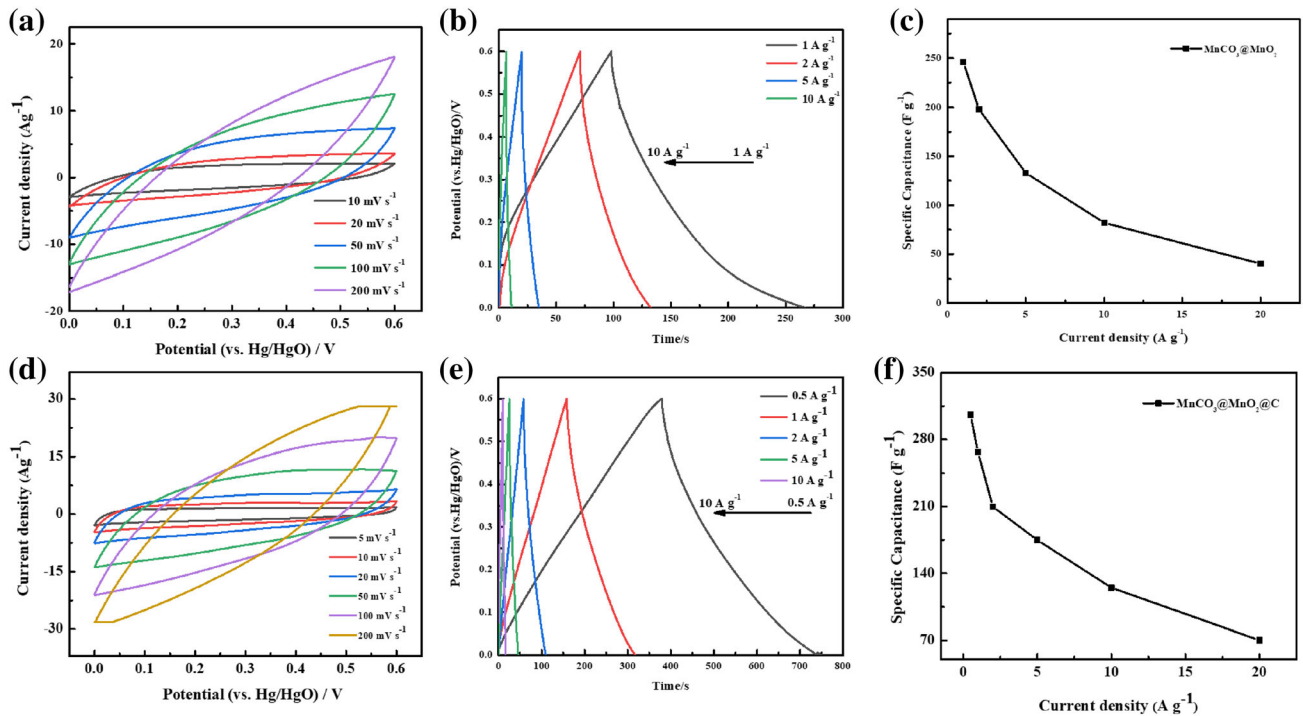


Fig. 4 The electrochemical properties of $\text{MnCO}_3@MnO_2$ and $\text{MnCO}_3@MnO_2@C$: **a, d** CV curves at different scanning speeds, **b, e** GCD curves at different current densities, **c, f** specific capacity calculated from GCD curves

$1 \text{ A}\cdot\text{g}^{-1}$, and has a 34.9% capacity retention at current density of $10 \text{ A}\cdot\text{g}^{-1}$. Moreover, $\text{MnCO}_3@MnO_2@C$ has a 49.8% capacity retention at current density of $10 \text{ A}\cdot\text{g}^{-1}$ and the specific capacitance is $267 \text{ F}\cdot\text{g}^{-1}$ at the current rate of $1 \text{ A}\cdot\text{g}^{-1}$. These electrical performance results shows that $\text{MnCO}_3@MnO_2@C$ has better specific capacity and rate capability compared with $\text{MnCO}_3@MnO_2$. As a comparison, Table 1 lists the relative performances of MnO_2 -based electrode materials and asymmetric supercapacitors (ASC) with previously reported literature, indicates that the exceptional electrochemical performance of $\text{MnCO}_3@MnO_2@C$ and demonstrates assembled $\text{MnCO}_3@MnO_2@C//\text{HCS}$ is a promising electrode in enhancing the performance of supercapacitors.

The capacitive performances of $\text{MnCO}_3@MnO_2$ and $\text{MnCO}_3@MnO_2@C$ electrode materials are shown in Fig. 5. In the CV curves of Fig. 5a, there is no obvious redox peaks is found, indicating that the electrode materials are charged and discharged at a quasi-constant rate. In the GCD tests of Fig. 5b, compared with $\text{MnCO}_3@MnO_2$, $\text{MnCO}_3@MnO_2@C$ shows a more symmetrical triangle, indicating that it has a higher coulomb efficiency and a smaller voltage drop. In the EIS test of Fig. 5c, it can be seen that $\text{MnCO}_3@MnO_2@C$ has a smaller internal resistance

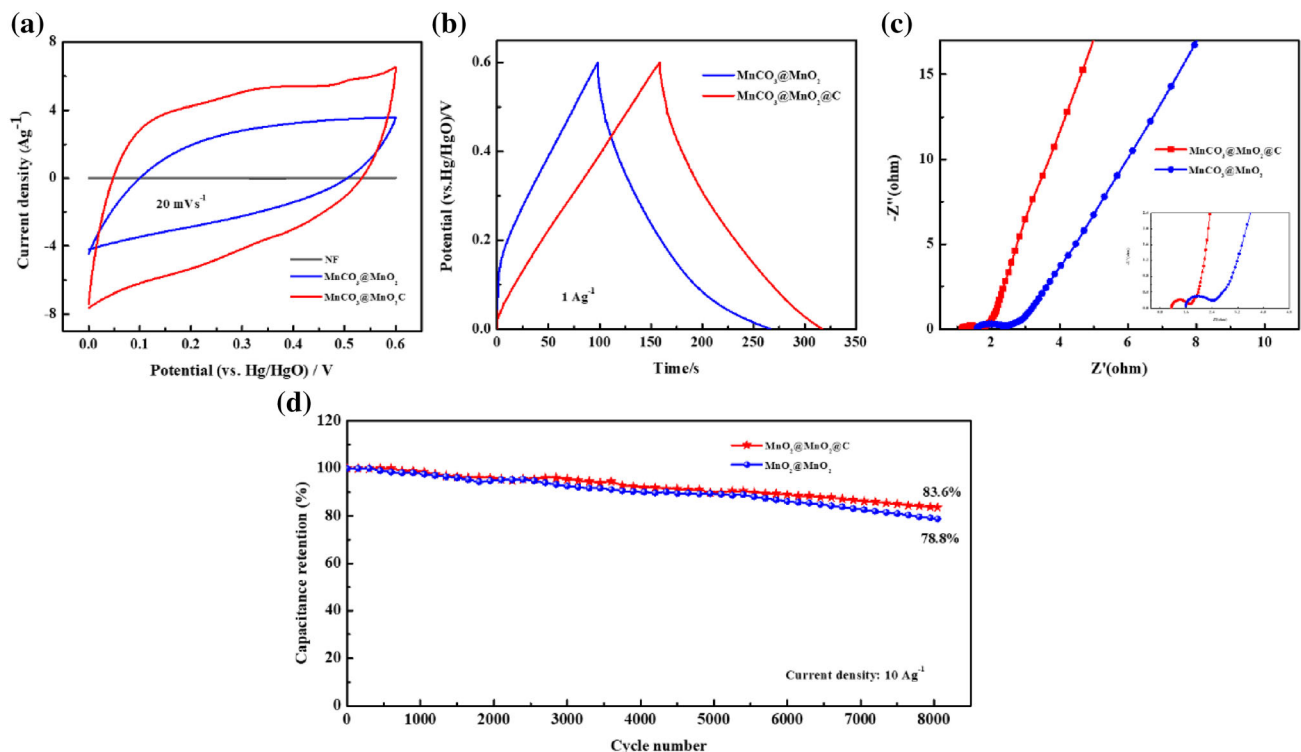
Rs than $\text{MnCO}_3@MnO_2$, indicating its interface resistance between the electrode and the current collector is smaller. In the low frequency region, it can be found that $\text{MnCO}_3@MnO_2@C$ has a bigger slope of the straight line than $\text{MnCO}_3@MnO_2$, indicating that it has a smaller diffusion resistance and capacitance. The reason of the results may be due to the synergistic effect of the increases in both conductivity of electrode material and utilization rate of manganese oxide lead by the coated carbon shell. Meanwhile, in the cycling stability of Fig. 5d, the capacity retention rates of $\text{MnCO}_3@MnO_2$ and $\text{MnCO}_3@MnO_2@C$ were excellent with 78.8% and 83.6% after 8000 cycles, respectively.

3.3 Electrochemical performance of supercapacitor

An asymmetric supercapacitor was fabricated using $\text{MnCO}_3@MnO_2@C$ and HCS as positive and negative electrodes, respectively. In Fig. 6a–c, the electrochemical properties of the HCS electrode were evaluated in 2 M KOH electrolyte among the voltage range is -1 to 0 V . The CV curve of the HCS presents a rectangular curve, which indicates that it has the characteristics of electric double layer

Table 1 Comparison the relative performances of MnO₂-based electrode materials and ASC with previously reported literature

Positive//negative electrodes	The specific capacitance of positive electrodes /(F g ⁻¹)	Electrolyte	Capacitance retention	Energy density /(Wh kg ⁻¹)	Power density /(W kg ⁻¹)	Ref.
MnCO ₃ @MnO ₂ //AG	363 (1A g ⁻¹)	1 M Na ₂ SO ₄	84.2% (1 A·g ⁻¹ , 2000)	27.4	4507.6	[31]
MnO ₂ /HCS//HCS	255 (1A g ⁻¹)	1 M Na ₂ SO ₄	93.9% (1 A·g ⁻¹ , 5000)	41.4	7901	[32]
γ-MnO ₂ /PANI//AC	216 (1A g ⁻¹)	1 M Na ₂ SO ₄	78.65% (5 A·g ⁻¹ , 3000)	66.4	350.1	[33]
MnO ₂ /rGO// rGO	242 (1A g ⁻¹)	1 M Na ₂ SO ₄	89.4% (1 A·g ⁻¹ , 1000)	21.2	820	[34]
MGA//GA	193.8 (1A g ⁻¹)	1 M Na ₂ SO ₄	84.1% (1.2 A·g ⁻¹ , 2000)	17.8	3200	[23]
MnCO ₃ @MnO ₂ @C//HCS	267 (1A g ⁻¹)	2 M KOH	78.2% (2 A·g ⁻¹ , 5000)	21.3	3840	This work

**Fig. 5** The electrochemical properties of MnCO₃@MnO₂ and MnCO₃@MnO₂@C electrode materials: **a** CV curves at 20 mV s⁻¹, **b** GCD curve at 1 A g⁻¹, **c**, **d** Nyquist plots and cycle stability

capacitance. The GCD curve shows that the specific capacity is 300 F·g⁻¹ at 1 A·g⁻¹. In the designed device, the weight of MnCO₃@MnO₂@C is 1.8 mg and that of HCS is 1 mg. Figure 6d is the CV curve of the MnCO₃@MnO₂@C and HCS electrode at a scan

rate of 20 mV·s⁻¹, showing a relatively rectangular shape. The voltage window of the assembled capacitor was speculated to be in the range of 0–1.7 V. CV tests of the assembled capacitor under voltage windows of 0–1.7 V at the scan of 20 mV·s⁻¹ was

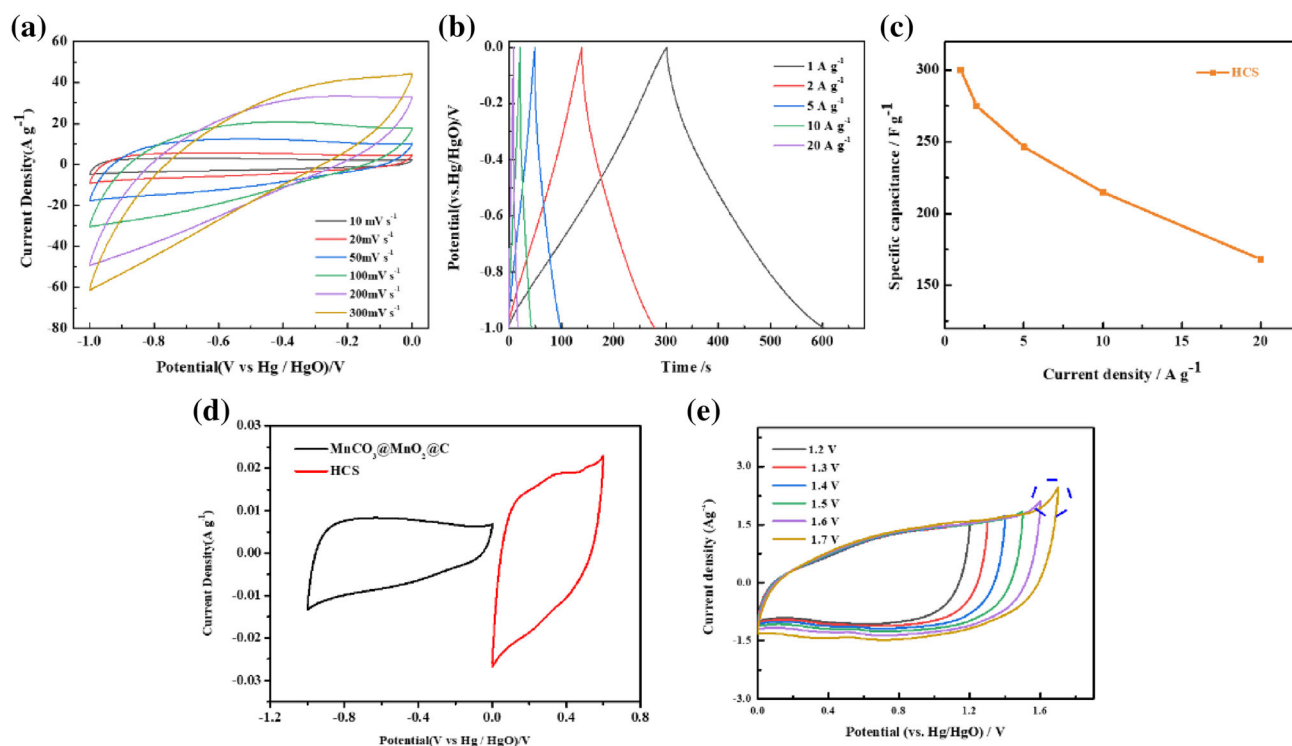


Fig. 6 **a** CV curves, **b** GCD curves and **c** specific capacity of HCS, **d** CV curve of $\text{MnCO}_3@\text{MnO}_2@\text{C}$ and HCS electrode materials at $20 \text{ mV}\cdot\text{s}^{-1}$, **e** CV curve of $\text{MnCO}_3@\text{MnO}_2@\text{C}/\text{HCS}$ asymmetric supercapacitor at $20 \text{ mV}\cdot\text{s}^{-1}$ in different voltage windows

performed in Fig. 6e. A sharp peak appears at the end of the CV curve, which indicates the precipitation of oxygen during the electrochemical measurement process and the ideal voltage window of the capacitors performance is about 0–1.6 V.

The electrochemical properties of the $\text{MnCO}_3@\text{MnO}_2@\text{C}/\text{HCS}$ asymmetric supercapacitors showing in Fig. 7a–c. All the CV curves at different scan rates varying from 5 to $200 \text{ mV}\cdot\text{s}^{-1}$ could be regarded to look like a rectangle shape. Meanwhile, as the scan rates increases, the integral area and peak current also increase, indicating that the assembled device has a good rate performance. All the GCD curves at a current density of $1 \text{ A}\cdot\text{g}^{-1}$ to $10 \text{ A}\cdot\text{g}^{-1}$ are relatively symmetrical triangles, showing the assembled device has a good capacitance characteristics and ideal coulomb efficiency. The specific capacitances of $\text{MnCO}_3@\text{MnO}_2@\text{C}/\text{HCS}$ calculated from Fig. 7b versus current density are presented in Fig. 7c. The specific capacitances is showed to be $60 \text{ F}\cdot\text{g}^{-1}$ at $1 \text{ A}\cdot\text{g}^{-1}$. Power density and energy density are two important parameters for evaluating the electrochemical performance of the supercapacitors. The energy density of $\text{MnCO}_3@\text{MnO}_2@\text{C}/\text{HCS}$ asymmetric supercapacitors is $21.3 \text{ Wh}\cdot\text{kg}^{-1}$ at power density of

$766.8 \text{ W}\cdot\text{kg}^{-1}$, and maintains $13.3 \text{ Wh}\cdot\text{kg}^{-1}$ at power density of $3840 \text{ W}\cdot\text{kg}^{-1}$. Afterward, the capacitance retention rate and coulomb efficiency diagram of $\text{MnCO}_3@\text{MnO}_2@\text{C}/\text{HCS}$ asymmetric supercapacitors at a current density of $2 \text{ A}\cdot\text{g}^{-1}$ was measured in Fig. 7d. The capacitors remained 78.2% of the capacitance retention of after 5000 cycles, and the coulomb efficiency is close to 100%, which indicating that $\text{MnCO}_3@\text{MnO}_2@\text{C}/\text{HCS}$ have a good rate performance.

4 Conclusion

In summary, $\text{MnCO}_3@\text{MnO}_2@\text{C}$ hierarchical hollow nanostructures are rationally prepared by used continuous redox reaction. Additionally, combined with the structural characteristics and electrochemical properties of the HCS, the $\text{MnCO}_3@\text{MnO}_2@\text{C}/\text{HCS}$ asymmetric supercapacitors are assembled. Benefiting from the carbon shell coating, the hollow shell MnO_2 surface plays a synergistic effect which increases conductivity of the electrode material and prevents the electrode material from powdering and agglomeration during the cycle. The results shows

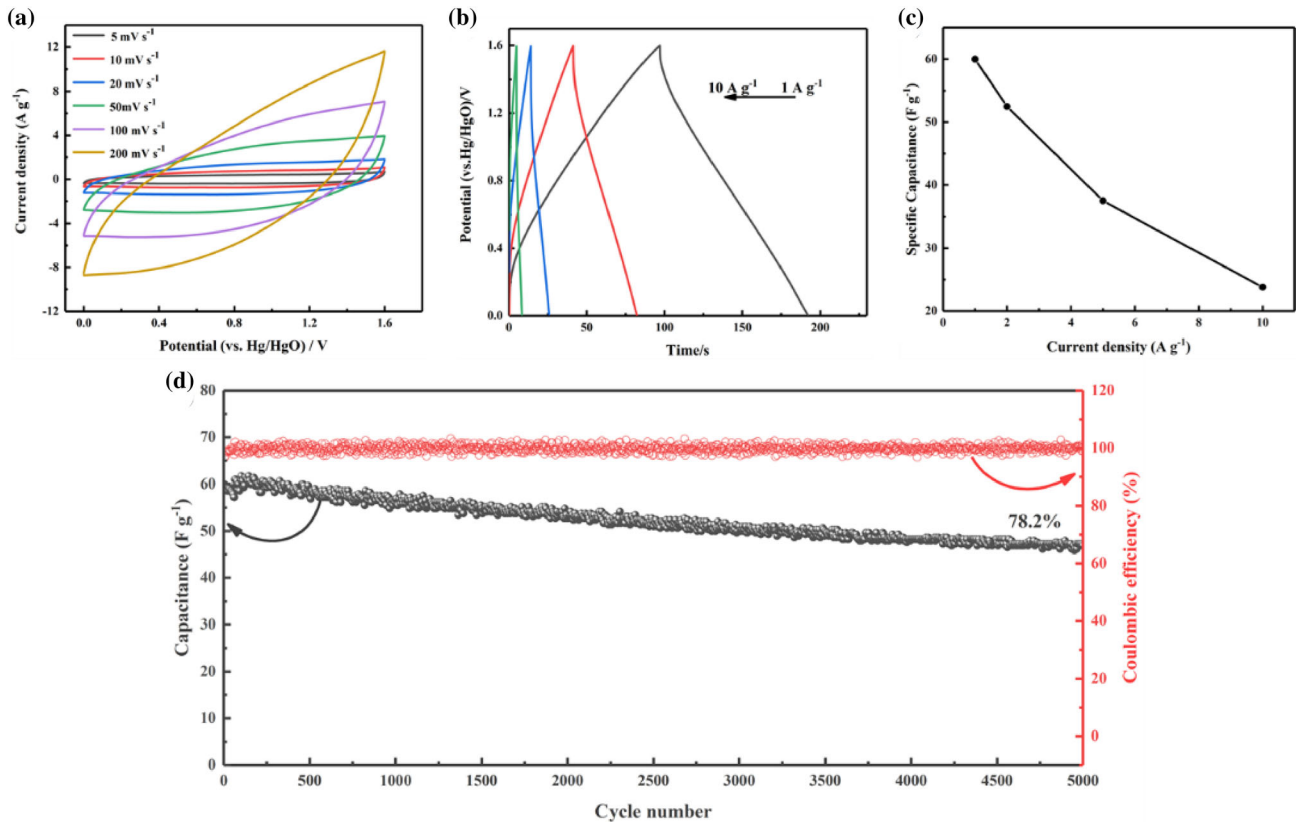


Fig. 7 The electrochemical properties of MnCO₃@MnO₂@C//HCS asymmetric supercapacitor: **a** CV curve at different scanning speeds, **b** GCD curve at different current densities, **c** specific

capacity at different current densities, **d** Capacitance retention rate and Coulomb efficiency

that the electrode material displays a specific capacitance of 267 F·g⁻¹ at current density of 1 A·g⁻¹ and 83.6% of the initial capacitance was retained after 8000 cycles at a current density of 10 A·g⁻¹. Meanwhile, the assembled capacitors display that the capacitance retention rate is 78.2% after 5000 cycles and the coulomb efficiency is close to 100% at current density of 2 A·g⁻¹. Furthermore, the maximum power density of 3840 W·kg⁻¹ and energy density of 21.3 Wh·kg⁻¹ are obtained.

Acknowledgements

This work is financially supported by the National Natural Science Foundation of China (21875141, U1760119), Science and Technology Commission of Shanghai Municipality (19DZ2271100), Shanghai Scientific and Technological Innovation Project (19JC1410400) and the Innovation Program of Shanghai Municipal Education Commission (2019-01-07-00-07-E00015).

References

1. Poonam, K. Sharma, A. Arora, S.K. Tripathi, Review of supercapacitors: Materials and devices. *J. Energy Storage* **21**, 801–825 (2019)
2. Z. Yang, J. Zhang, M.C. Kintner-Meyer, X. Lu, D. Choi, J.P. Lemmon, J. Liu, Electrochemical energy storage for green grid. *Chem. Rev.* **111**, 3577–3613 (2011)
3. L.L. Zhang, X.S. Zhao, Carbon-based materials as supercapacitor electrodes. *Chem. Soc. Rev.* **38**, 2520–2531 (2009)
4. M. Huang, F. Li, F. Dong, Y.X. Zhang, L.L. Zhang, MnO₂-based nanostructures for high-performance supercapacitors. *J. Mater. Chem. A* **3**, 21380–21423 (2015)
5. P. Naskar, A. Maiti, P. Chakraborty, D. Kundu, B. Biswas, A. Banerjee, Chemical supercapacitors: a review focusing on metallic compounds and conducting polymers. *J. Mater. Chem. A* **9**, 1970–2017 (2021)
6. Z. Wang, L. Zhou, X.W. Lou, Metal oxide hollow nanostructures for lithium-ion batteries. *Adv Mater* **24**, 1903–1911 (2012)
7. Y.E. Miao, W. Fan, D. Chen, T. Liu, High-performance supercapacitors based on hollow polyaniline nanofibers by

- electrospinning. *ACS Appl Mater Interfaces* **5**, 4423–4428 (2013)
8. M.R. Arcila-Velez, M.E. Roberts, Redox solute doped Polypyrrole for high-charge capacity polymer electrodes. *Chem. Mater.* **26**, 1601–1607 (2014)
 9. T. Liu, L. Finn, M. Yu, H. Wang, T. Zhai, X. Lu, Y. Tong, Y. Li, Polyaniline and polypyrrole pseudocapacitor electrodes with excellent cycling stability. *Nano Lett.* **14**, 2522–2527 (2014)
 10. Y. Wang, Y. Ding, X. Guo, G. Yu, Conductive polymers for stretchable supercapacitors. *Nano Res.* **12**, 1978–1987 (2019)
 11. Y. Wang, J. Guo, T. Wang, J. Shao, D. Wang, Y.W. Yang, Mesoporous transition metal oxides for supercapacitors. *Nanomaterials (Basel)* **5**, 1667–1689 (2015)
 12. X. Lang, A. Hirata, T. Fujita, M. Chen, Nanoporous metal/oxide hybrid electrodes for electrochemical supercapacitors. *Nat Nanotechnol* **6**, 232–236 (2011)
 13. A.U. Ubale, M.A. Waghmare, K.S. Iqbal, H.M. Pathan, Manganese oxides: promising electrode materials for Li-ion batteries and supercapacitors. *J. Mater. Sci.: Mater. Electron.* **31**, 14003–14021 (2020)
 14. H. Gao, F. Xiao, C.B. Ching, H. Duan, High-performance asymmetric supercapacitor based on graphene hydrogel and nanostructured MnO₂. *ACS Appl Mater Interfaces* **4**, 2801–2810 (2012)
 15. K. Lota, V. Khomenko, E. Frackowiak, Capacitance properties of poly(3,4-ethylenedioxythiophene)/carbon nanotubes composites. *J. Phys. Chem. Solids* **65**, 295–301 (2004)
 16. Y. Huang, H. Li, Z. Wang, M. Zhu, Z. Pei, Q. Xue, Y. Huang, C. Zhi, Nanostructured Polypyrrole as a flexible electrode material of supercapacitor. *Nano Energy* **22**, 422–438 (2016)
 17. J. Xiao, J. Han, C. Zhang, G. Ling, F. Kang, Q.H. Yang, Dimensionality, function and performance of carbon materials in energy storage devices. *Adv. Energy Mater* (2021). <https://doi.org/10.1002/aenm.202100775>
 18. S. Li, A. Pasc, V. Fierro, A. Celzard, Hollow carbon spheres, synthesis and applications—a review. *J. Mater. Chem. A* **4**, 12686–12713 (2016)
 19. S.A. Abbas, M. Forghani, S. Anh, S.W. Donne, K.-D. Jung, Carbon hollow spheres as electrochemical capacitors: Mechanistic insights. *Energy Storage Mater.* **24**, 550–556 (2020)
 20. J.B. Fei, Y. Cui, X.H. Yan, W. Qi, Y. Yang, K.W. Wang, Q. He, J.B. Li, Controlled preparation of MnO₂ hierarchical hollow nanostructures and their application in water treatment. *Adv. Mater.* **20**, 452–456 (2008)
 21. Y. Yin, R.M. Rioux, C.K. Erdonmez, S. Hughes, G.A. Somorjai, A.P. Alivisatos, Formation of hollow nanocrystals through the nanoscale Kirkendall effect. *Science* **304**, 711–714 (2004)
 22. X. Wang, J. Feng, Y. Bai, Q. Zhang, Y. Yin, Synthesis, properties, and applications of hollow micro-/nanostructures. *Chem. Rev.* **116**, 10983–11060 (2016)
 23. Y. Liu, D. He, H. Wu, J. Duan, Y. Zhang, Hydrothermal self-assembly of manganese dioxide/manganese carbonate/reduced graphene oxide aerogel for asymmetric supercapacitors. *Electrochim. Acta* **164**, 154–162 (2015)
 24. H. Zhang, O. Noonan, X. Huang, Y. Yang, Surfactant-free assembly of mesoporous carbon hollow spheres with large tunable pore sizes. *ACS Nano* **10**, 4579 (2016)
 25. W. Lu, Y. Li, M. Yang, X. Jiang, Y. Zhang, Y. Xing, Construction of hierarchical Mn₂O₃@MnO₂ core-shell nanofibers for enhanced performance supercapacitor electrodes. *ACS applied energy materials* **3**, 8190–8197 (2020)
 26. J. Stejskal, M. Trchová, Conducting polypyrrole nanotubes: a review. *Chem. Pap.* **72**, 1563–1595 (2018)
 27. L.Q. Liu, J.M. Wang, M.Y. Wu, Y.K. Fan, Physical properties and electrochemical performance of γ -MnO₂ with ultrafine powder. *J. Funct. Mater.* **36**, 404–407 (2005)
 28. Z. Fan, J. Yan, W. Tong, L. Zhi, G. Ning, T. Li, W.J.A.F.M. Fei, Asymmetric supercapacitors based on Graphene/MnO₂ and activated carbon nanofiber electrodes with high power and energy density. *Adv. Funct. Mater* **21**, 2366–2375 (2011)
 29. N. Jin, M. Liu, X. Feng, Z. Zhang, M. Dou, W.J.C. Feng, Synchronously boosting gravimetric and volumetric performance: Biomass-derived ternary-doped microporous carbon nanosheet electrodes for supercapacitors. *Carbon* **140**, 664–672 (2018)
 30. L. Zhang, X. Yu, L. Lv, P. Zhu, F. Zhou, G. Li, R. Sun, C.-P. Wong, Ultrathin manganese dioxide nanosheets grown on mesoporous carbon hollow spheres for high performance asymmetrical supercapacitors. *ACS Applied Energy Materials* **10**, 5402–5409 (2018)
 31. H. Chen, Z. Yan, X.Y. Liu, X.L. Guo, Y.X. Zhang, Rational design of microsphere and microcube MnCO₃@MnO₂ heterostructures for supercapacitor electrodes. *J. Power Sources* **353**, 202–209 (2017)
 32. W. Du, X. Wang, J. Zhan, X. Sun, L. Kang, F. Jiang, X. Zhang, Q. Shao, M. Dong, H. Liu, V. Murugadoss, Z. Guo, Biological cell template synthesis of nitrogen-doped porous hollow carbon spheres/MnO₂ composites for high-performance asymmetric supercapacitors. *Electrochim. Acta* **296**, 907–915 (2019)
 33. Y. Zhu, H. Xu, J. Tang, X. Jiang, Y. Bao, Y. Chen, Synthesis of γ -MnO₂/PANI Composites for Supercapacitor Application in Acidic Electrolyte. *J. Electrochem. Soc.* **168**, 030542 (2021)

34. S. Wu, W. Chen, L. Yan, Fabrication of a 3D MnO₂/graphene hydrogel for high-performance asymmetric supercapacitors. *J. Mater. Chem. A* **2**, 2765 (2014)

Publisher's Note Springer Nature remains neutral with regard to jurisdictional claims in published maps and institutional affiliations.